The following publication J. Zhu, K. W. E. Cheng and X. Xue, "Design and Analysis of a New Enhanced Torque Hybrid Switched Reluctance Motor," in IEEE Transactions on Energy Conversion, vol. 33, no. 4, pp. 1965-1977, Dec. 2018 is available at https://doi.org/10.1109/TEC.2018.2876306.

Design and Analysis of a New Enhanced Torque Hybrid Switched Reluctance Motor

Jingwei Zhu, Ka Wai Eric Cheng, *Senior Member, IEEE,* Xiangdang Xue, *Senior Member, IEEE*

***Abstract*--In this paper, a new 6/10 hybrid switched reluctance motor (HSRM) is proposed. This original topology deploys permanent magnets (PMs) between adjacent stator poles of a divided teeth SRM. The function of the PMs is to weaken the magnetic saturation in stator poles, which is a major obstacle of torque improvement for divided teeth SRMs. Besides, the magnetic flux in the airgap increases as well. Hence, the output torque can be increased significantly. The flux distribution of the topology is analyzed by using equivalent magnetic circuit (EMC). The topology is optimized by using genetic algorithm (GA) for the best torque performance. Additionally, the characteristics of the proposed topology are compared with a 12/10 SRM, a 6/10 two-teeth SRM, a 12-slot, 10-pole three-phase six-state PM brushless DC motor (BLDCM) and a flux switching permanent magnet motor (FSPM) of the same dimension. A prototype of the proposed topology is manufactured for experimental verification. The simulation and experimental results indicate that the proposed topology can achieve high torque density and high PM utilization factor simultaneously.**

***Index Terms*—Cogging torque, hybrid excitation, multiple teeth, parameter optimization, switched reluctance motor, torque density**

I. Introduction

THE switched reluctance motor (SRM) has attracted much attentions in vehicular and industrial fields as a dynamical source [1]-[3]. Its preferred features of simple and robust structure, no windings on the rotor and elimination of permanent magnet (PM) material are quite necessary in extremely harsh industrial condition. Besides, its other advantages of low cost, fault tolerance and wide operation speed range have been utilized for extensive applications [4]-[6]. Additionally, the structure of asymmetric bridge for power converters enhances the operation stability and phase independence compared with the three-phase bridge [7].

A great deal of research has been conducted in this area in the past few decades, including the nonlinear magnetic field and power converter. A nonlinear model of the SRM is proposed in [8] to achieve accurate calculation of core loss. A position stepping method [9] is introduced to solve the problem of nonlinear relationship between torque, excitation current and position within CPU execution time. A new torque estimator for SRM drives [10] is presented to rapidly estimate the instantaneous output torque. An asymmetric three-level neutral point diode clamped converter is analyzed to improve the motor performance in [11]. An integrated multiport power converter [12] is put forward to reduce value of the DC capacitor. To lower the DC-link ripples, an interleaved DC-DC converter is proposed [13].

However, the low torque density characteristic limits its usage for high torque application, which has attracted numerous scholars to investigate in depth. Segmented stator or rotor topology is an efficient method to improve torque output by utilizing short magnetic paths or different excitation strategies [14]-[17], but it increases the manufacturing difficulty and lowers the accuracy. Some modified structures of SRMs have also been proposed to enhance torque performance, including double layer per phase [18], double stator [19] and axial type SRMs [20], [21], but all of them are at the expenses of sacrificing the simple and robust structure. A topology of two teeth per stator pole is put forward to increase the output torque [22]; the extremely high magnetic saturation in the stator pole and relatively smaller slot area, however, limit high torque output and cause high torque ripple. An improved two teeth topology with more rotor poles than stator teeth is analyzed in [23], but it is not suitable for high speed applications.

Although extensive research has been conducted on PM motors for high torque output [24], [25], there is unavoidable cogging torque in PM motors and quite considerable amount of PM poles are used, resulting in much higher cost. A new type of flux switching permanent magnet motor (FSPM) with PM inserted into the stator pole is proposed [26]. This kind of machine has the advantage of maintain a simple and robust rotor structure. However, it possesses a poor utilization of PM material due to high level of magnetic saturation in the stator part [27]. Moreover, the existence of PMs leads to insufficient area for windings, which limits the torque output [28]. The idea of inserting PMs into SRMs to improve the torque performance with little cogging torque is implemented in [29], [30], but the manufacturing process for stator segmented topology is difficult and the normal operation of high magnetic saturation for SRMs restricts the flux increase in the airgap. Therefore, the torque enhancement is quite limited. Ding [31] presents an improved SRM topology with PM assisted excitation, but the amount of PM material is quite substantial to achieve high torque output.

This paper presents a new hybrid switched reluctance motor (HSRM) by inserting PM material between adjacent stator poles of a two teeth SRM. The configuration of the topology is

Manuscript received December 21, 2017. This work was supported by the Research Committee of The Hong Kong Polytechnic University under the project: G-YBLH

The authors are with The Hong Kong Polytechnic University, Hung Hom, Kowloon, Hong Kong, China. (email: jingwei.zhu@connect.polyu.hk; eeecheng@polyu.edu.hk; xd.xue@polyu.edu.hk)

introduced. Then, the working principle is analyzed by utilizing equivalent magnetic circuit (EMC) model. Besides, the motor parameters are optimized for the best performance. The characteristics are compared with those of 12/10 SRM, two teeth SRM with no PMs, 12-slot, 10-pole three-phase six-state PM brushless DC motor (BLDCM) and a 12/10 FSPM. Eventually, a prototype is manufactured for experimental tests in order to verify the proposed design.

II. Configuration of the HSRM

The structure of the proposed topology is shown in Fig. 1. It is a three-phase 6/10 HSRM with two teeth per stator pole. The PMs are set between adjacent stator poles and the magnetization directions of PMs are represented by the red arrows. The novel topology exhibits numerous advantageous features:

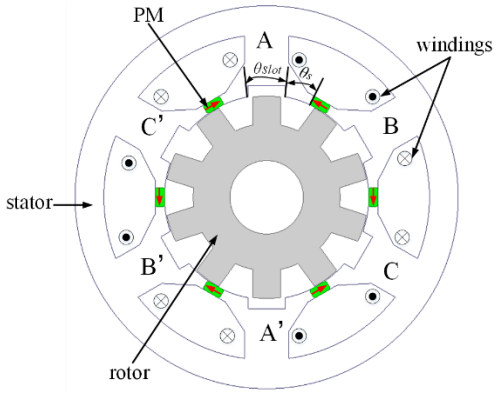

Fig. 1. Configuration of the proposed motor

1) *Concentrated field windings*: be simple, save copper material and shorten the winding end length.
2) *Multiple teeth per stator pole*: [32] illustrates multi-tooth topology for torque improvement in SRMs. As proved in [14] and [23], two teeth topology exhibits the best torque performance. The electromagnetic torque of *m* teeth per stator pole SRM can be calculated as [23],

$$T_e = \int_0^I \frac{N^2 I \mu_0 mlr}{2l_g} dI = \frac{N^2 I^2 \mu_0 mlr}{4l_g} \quad (1)$$

where l_g and l is the airgap and stack length, respectively; N is number of turns per phase and μ_0 is magnetic permeability in the vacuum. Therefore, the proposed design will enhance the torque output through increase in m.

3) *Magnetic flux regulating ability of PM material*: the functions of PMs are to lower the magnetic saturation level in the stator pole to prevent high magnetic reluctance and contribute to the flux increase in the airgap, leading to torque improvement.

III. Analysis of Working Principle

A. Structure Analysis

As shown in Fig. 1, the novel motor, consisting of three phases named AA′, BB′ and CC′, adopts the conducting mode and winding configuration of conventional SRMs, with one or two phases conducting at the same time. The winding configuration is illustrated in Fig. 2 (b). The number of rotor poles is selected as ten. The flux distributions under non-excitation and current excitation conditions are shown in Fig. 2 (a) and (b) respectively, where Φ_{PM}, Φ_{pole} and Φ_{air} is the magnetic flux flowing through the PM, stator pole and airgap, respectively. When there is no current excitation, the major part of the magnetic flux flows through the stator. When there is current excitation, the flux produced by the PM will go through the stator pole and airgap, separately, thus, it weakens the flux density in the stator pole and increases the flux in the airgap. By utilizing FEM, the flux distributions of the whole motor at the aligned position under excitation and non-excitation condition, can be observed from Fig. 3 (a) and (b), respectively.

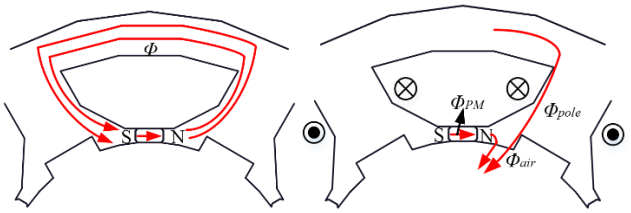

Fig. 2. Flux distribution with (a) non-excitation (b) excitation

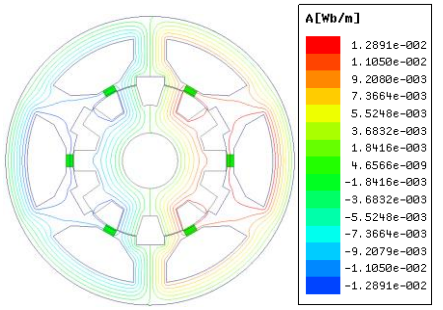

(a)

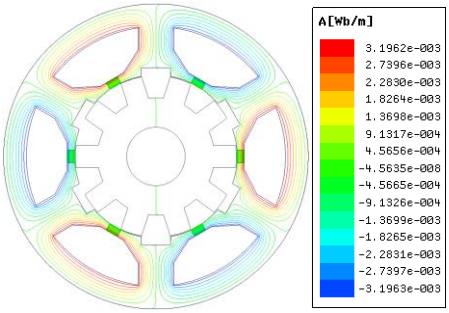

(b)

Fig. 3. Flux distribution (a) with field current (b) without field current at the aligned position of the whole machine

B. EMC Model of the Proposed Machine

The EMC model is quite efficient to analyze electric machines [33]. The magnetic circuit model under phase A excitation condition is demonstrated in Fig. 4 (a), neglecting the mutual and leakage inductance [34]. As illustrated in Fig. 4 (a), since the configuration of the topology is bilaterally symmetric, the left half part is considered for theoretical analysis and the equivalent magnetic circuit can be transferred to Fig. 4 (b), where F_p and F_i is the magneto motive force

(MMF) provided by PM and field current per phase, respectively; R_g, R_r, R_p, R_{sp} and R_{sy} is the magnetic reluctance of the airgap, rotor, PM, stator pole and stator yoke, separately. R_{g1} is the sum of reluctance of two airgaps.

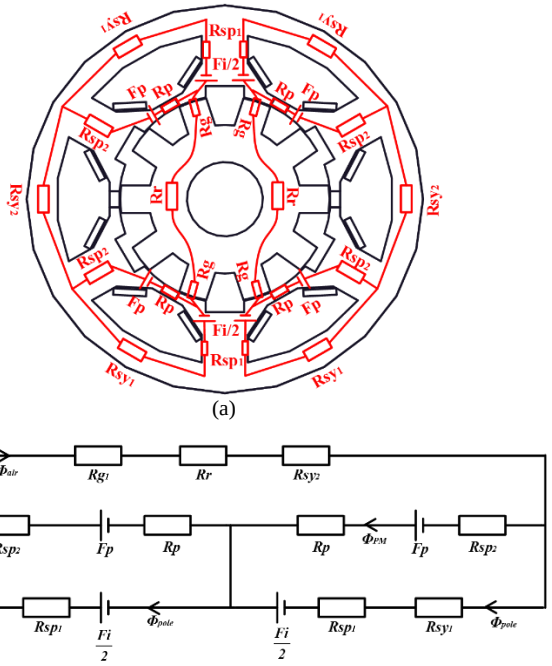

Fig. 4. (a) Magnetic circuit model under excitation condition (b) simplified magnetic circuit of the proposed topology

With Kirchhoff laws (KVL and KCL) considered, the equations of magnetic circuit are expressed as

$$\begin{cases} \Phi_{air} = \Phi_{pole} + \Phi_{PM} \\ F_i = \Phi_{air}(R_{g1} + R_r + R_{sy2}) + 2\Phi_{pole}(R_{sp1} + R_{sy1}) \\ 0.5F_i - \Phi_{pole}(R_{sy1} + R_{sp1}) = F_p - \Phi_{PM}(R_p + R_{sp2}) \end{cases} \quad (2)$$

The result can be solved as

$$\begin{cases} \Phi_{pole} = \dfrac{F_i[R_{g1} + R_r + R_{sy2} + 2(R_p + R_{sp2})]}{2\boldsymbol{R}} - \dfrac{F_p(R_{g1} + R_r + R_{sy2})}{\boldsymbol{R}} \\ \Phi_{air} = \dfrac{F_i(R_p + R_{sp2})}{\boldsymbol{R}} + \dfrac{2F_p(R_{sp1} + 2R_{sy1})}{\boldsymbol{R}} \\ \Phi_{PM} = \dfrac{F_p(R_{g1} + R_r + R_{sy2} + 2R_{sp1} + 2R_{sy1})}{\boldsymbol{R}} - \dfrac{F_i(R_{g1} + R_r + R_{sy2})}{2\boldsymbol{R}} \end{cases} \quad (3)$$

where

$$\boldsymbol{R} = (R_p + R_{sp2})(R_{g1} + R_r + R_{sy2} + 2R_{sp1} + 2R_{sy1}) + (R_{g1} + R_r + R_{sy2})(R_{sy1} + R_{sp1})$$

.

Due to R_p>>$(R_{sy1}+R_{sp1})$ and $2(R_p+R_{sp2})$>>$(R_{g1}+R_r+R_{sy2})$,

$$\boldsymbol{R} \approx (R_p + R_{sp2})(R_{g1} + R_r + R_{sy2} + 2R_{sp1} + 2R_{sy1}) \quad (4)$$

$$R_{g1} + R_r + R_{sy2} + 2(R_p + R_{sp2}) \approx 2(R_p + R_{sp2}) \quad (5)$$

the result can be simplified as

$$\Phi_{pole} \approx \frac{F_i}{R_{g1} + R_r + R_{sy2} + 2(R_{sp1} + R_{sy1})} - \frac{F_p(R_{g1} + R_r + R_{sy2})}{\boldsymbol{R}} \quad (6)$$

$$\Phi_{air} \approx \frac{F_i}{R_{g1} + R_r + R_{sy2} + 2(R_{sp1} + R_{sy1})} + \frac{2F_p(R_{sp1} + R_{sy1})}{\boldsymbol{R}} \quad (7).$$

For the topology without PMs, Φ_{pole} and Φ_{air} can be calculated as

$$\Phi_{pole} = \Phi_{air} = \frac{F_i}{R_{g1} + R_r + R_{sy2} + 2(R_{sp1} + R_{sy1})} \quad (8)$$

Therefore, from (6), (7) and (8), the functions of PMs are proved to lower the magnetic saturation in the stator pole and increase the flux density in the airgap by redistributing the magnetic flux lines. Furthermore, due to the fact that $(R_{g1}+R_r+R_{sy2})$>>$2(R_{sp1}+R_{sy1})$, the decrease in flux density in the stator pole is much more significant than the increase in the airgap. However, with the rotor moving from the unaligned position to the aligned one, the value of R_{g1} decreases gradually, allowing more magnetic flux produced by PMs to flow into the airgap rather than into the stator pole. Also, the PM material will not endure demagnetization if it meets the condition of $2F_p$>F_i.

IV. Design Consideration & Optimization

Although the working principle of the proposed topology has been discussed in Section II, some design considerations and optimization strategies are required to maintain the best operating performance. Some parameter optimization methods are conducted in [31], [35], but they are not suitable for multi-variable optimization. The reason is that all the other parameters are kept constant if just one parameter is being optimized. Genetic algorithm (GA) is a common method for motor parameter optimization, especially for multiple variables and multi-objective [14]. The design strategy of this machine involves the above two methods. The parameters of the PM thickness γ and the stator inner slot depth h_{s1} are not easy to be included in the fitness function, so the first method is utilized for optimization. Other parameters, including the stator inner diameter D_{s1}, rotor pole height h_r, stator yoke thickness b_s, stator teeth arc angle θ_s, rotor pole arc angle β_r and l_1, l_2, α as demonstrated in Fig. 5, are optimized by using GA method. The stator outer diameter, stack length and airgap length are kept constant, with the value of 120 mm, 85 mm and 0.3 mm, respectively.

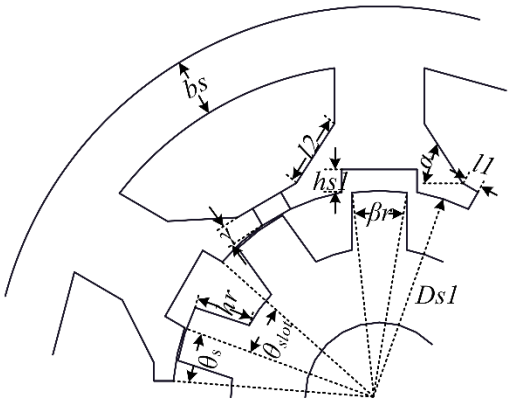

Fig. 5. Major dimension parameters of the proposed motor

A. Optimization of the Thickness of PMs

Due to the fact that PM acts as a significant role in modulating the magnetic flux in the stator and airgap, the thickness of PMs γ should be analyzed for its effect on torque performance. The flux linkage curves at the aligned and unaligned positions with different values of γ on the basis of finite element analysis (FEA) can be obtained from Fig. 6 (a). When there is no current, the flux linkage is negative in the stator pole, corresponding to the theoretical analysis. Also, the average torque curves with different values of PM thickness can be found in Fig. 6 (b). It illustrates that when γ exceeds 3 mm, the torque improvement is quite limited. Moreover, for the proposed motor, the rated current value in square wave form is around 10 A, contributing to the highest torque performance of that with 3 mm thick PMs. When PMs become thicker, not only the cost of the machine increases, but some winding areas are occupied as well, leading to lower torque output. However, when the value of current becomes larger, thicker PMs have the advantage of allowing more magnetic flux to flow into the airgap, thus, improving the torque performance. Therefore, considering the normal operation of the machine, the thickness is settled as 3 mm.

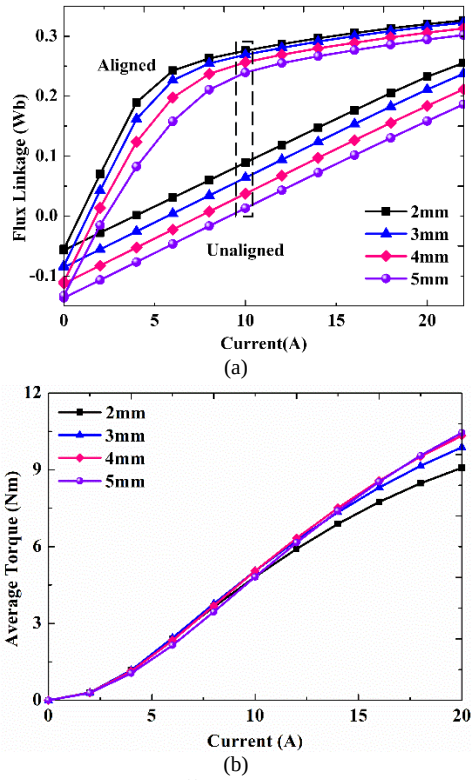

Fig. 6. (a) Flux linkage with different PM thickness (b) Average torque of different γ with various excitation current

B. Influence of the Stator Inner Slot Depth

The stator inner slot depth (h_{s1}) also has considerable impacts on the motor performance. If it is too shallow, magnetic flux leakage will be high enough to weaken the torque performance. On the other hand, if it is fairly deep, some parts of the stator pole will be seriously magnetic saturated to decline the efficiency. As a result, a suitable depth is required for the best performance of operation. The values of 1.5 mm, 2 mm, 2.5 mm, 3 mm, 3.5 mm and 4 mm are chosen for comparison by utilizing FEA. Their average torque curves can be obtained from Fig. 7. The comparison results show that the depth of 3 mm contributes to the best torque performance. Higher or lower value of the depth will weaken the performance just as the former analysis. As a consequence, the optimal stator inner slot depth is set as 3 mm.

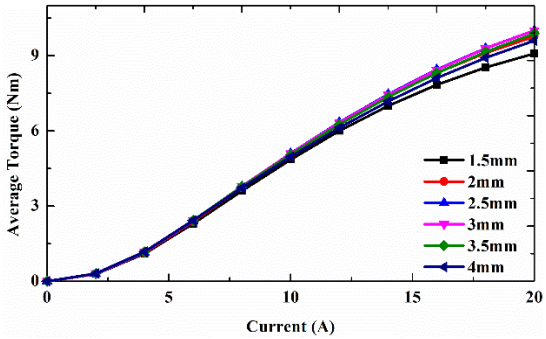

Fig. 7. Average torque of different h_{s1} with various excitation current

C. GA Method for Multi-variable Optimization

For other motor parameters, the method changing one and keeping the others constant is not suitable for the optimal parameter combination. Therefore, the GA method is brought into the limelight since these parameters are much easier to set up a fitness function for optimization.

For this two-teeth each stator pole 6/10 HSRM, it should satisfy

$$\theta_{slot} + \theta_s = \frac{2\pi}{N_r} \tag{9}$$

where θ_{slot} is the stator inner slot arc angle as shown in Fig. 5 and N_r is the number of rotor poles. The commutation angle for this topology is 12 degree. To obtain the best torque performance, the optimization objective is to improve the average torque and reduce torque ripple. Torque ripple can be expressed as

$$T_{ripple} = \frac{T_{max} - T_{min}}{T_{avg}} \cdot 100\% \tag{10}$$

As a result, the fitness function is selected as

$$F = 150 \cdot (0.7 \cdot T_{avg} - 0.3 \cdot T_{ripple} \cdot T_{avg}) \tag{11}$$

where *0.7* and *0.3* is the weight coefficient of average torque and torque ripple, respectively, for the contribution to the fitness function value; *150* is the multiplier for larger fitness value. The conducting mode is that each phase is excited in half an electrical period. The average torque is an average value of torque at different positions. The mutual coupling effect between phases and inductance leakage can be neglected [30]. Therefore, the average torque is calculated as

$$T_{avg} = \frac{1}{2} \cdot \frac{(L_a - L_u) \cdot N_r}{\pi} \cdot I^2 \tag{12}$$

where L_a and L_u are the inductance values at aligned and unaligned positions, respectively. Their values can be acquired accurately by using equivalent magnetic circuit to analyze various kinds of flux lines passing through the machine [36]. Moreover, due to the air cooling condition, the current density is limited to 5.5 A/mm^2. As a result of concentrated winding,

the slot filling factor is set as 0.4. Also, other design constraints for SRMs [36] should be considered for the proposed motor.

The process of GA method can be obtained from the flowchart in Fig. 8. For GA optimization, the population number is 50, the maximum generation number is 15, the crossover probability is 0.8 and the mutation is 0.06. For selection process, stochastic uniform is utilized. Elite count is able to go into the next generation directly to accelerate the optimization procedure and its number is set as 2. Through GA optimization, the average and best fitness value during the optimization are shown in Fig. 9. The result indicates that with the generation number increasing, the best fitness value increases and finally becomes stable, even though the mean fitness value endures some fluctuation.

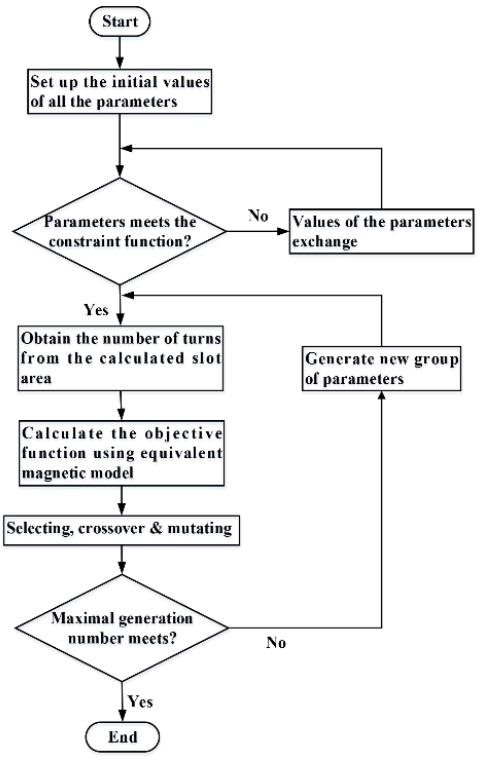

Fig. 8. Process of GA optimization

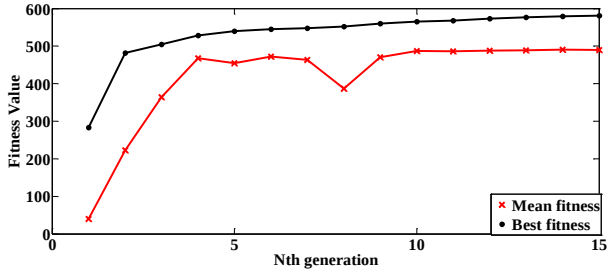

Fig. 9. Fitness value during GA optimization

The final optimized parameters through GA optimization are shown in Table I. Therefore, the overall dimensions of the proposed HSRM are determined. The electromagnetic characteristics of the machine are analyzed by 2D-FEA. Fig. 10 (a) and (b) demonstrate the magnetic flux density at the positions of non-alignment and alignment, respectively, with the rated phase A current (current density 5.5 A/mm^2). The angle between the aligned and unaligned positions is 18 degree. The average flux density in the stator pole is about 1.5 T and the peak value near the stator teeth is around 2.1 T at the aligned position. Besides, the relationship between the flux linkage and current at different positions can be obtained from Fig. 11 (a). Additionally, the static torque performance with various excitation currents injected into phase A is shown in Fig. 11 (b).

TABLE I
OPTIMIZED MOTOR PARAMETERS

Parameter	Value	Parameter	Value
D_{s1} (mm)	64	β_r (degree)	15.5
h_r (mm)	8.8	l_1 (mm)	2.76
b_s (mm)	9	l_2 (mm)	10.84
θ_s (degree)	15	α (degree)	57

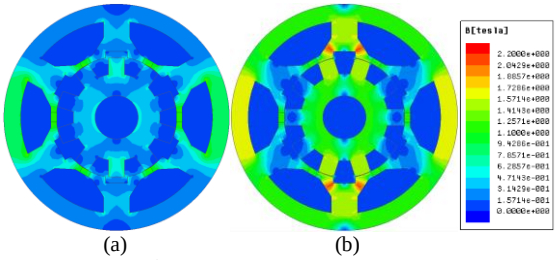

(a) (b)

Fig. 10. Magnetic flux density at (a) unaligned (b) aligned position

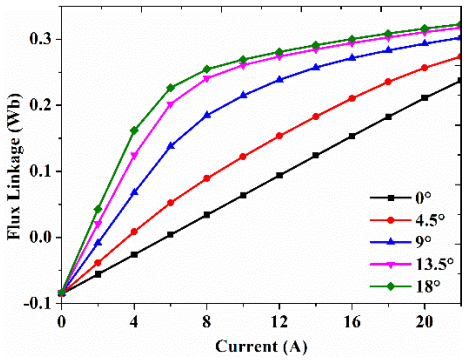

(a)

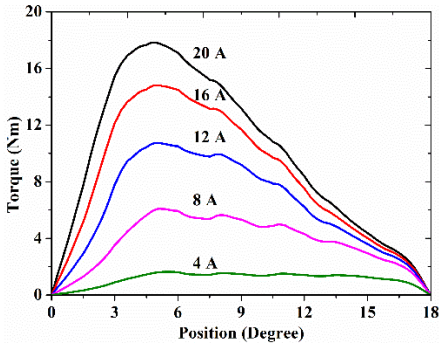

(b)

Fig. 11. Motor characteristics (a) Flux linkage curves of the proposed topology (b) Static torque performance of the proposed topology

V. PERFORMANCE COMPARISON WITH OTHER MOTORS

In order to confirm the advantageous features of the novel topology, a 12/10 SRM and a 6/10 two teeth SRM are proposed for comparison in torque performance. Meanwhile, a 12-slot 10-pole three-phase six-state PM BLDCM and a 12/10 FSPM are also proposed for comparison in the aspect of PM

utilization factor. All the motors are optimized and of the same dimension. The configurations of the five topologies are shown in Fig. 12.

A. Comparison with SRMs

To test the torque performance improvement of the proposed machine, it is first compared with 12/10 SRM and 6/10 two teeth SRM. All the candidates for comparison are three-phase motors. The 6/10 two teeth SRM is considered as a counterpart to prove the torque improvement produced by PMs, while the 12/10 SRM is utilized to confirm the superiority of the proposed machine over conventional three-phase SRMs. The magnetic flux density of the counterparts at unaligned and aligned positions with the rated current value can be found in Fig. 13. The average flux density in the stator pole of 12/10 SRM is about 1.65 T. Fig. 10 (a), (b) and Fig. 13 (c), (d) together show that the novel machine can weaken the flux density by 0.15 T and 0.45 T at the aligned and unaligned positions, respectively. From Fig. 13 (e) and (f), the comparison of flux density at the position of alignment demonstrates that the proposed motor is able to increase the flux density by 0.3 T in the airgap. Therefore, both the decreased core reluctance in the stator pole and the increased flux density in the airgap devote to the improvement of torque output.

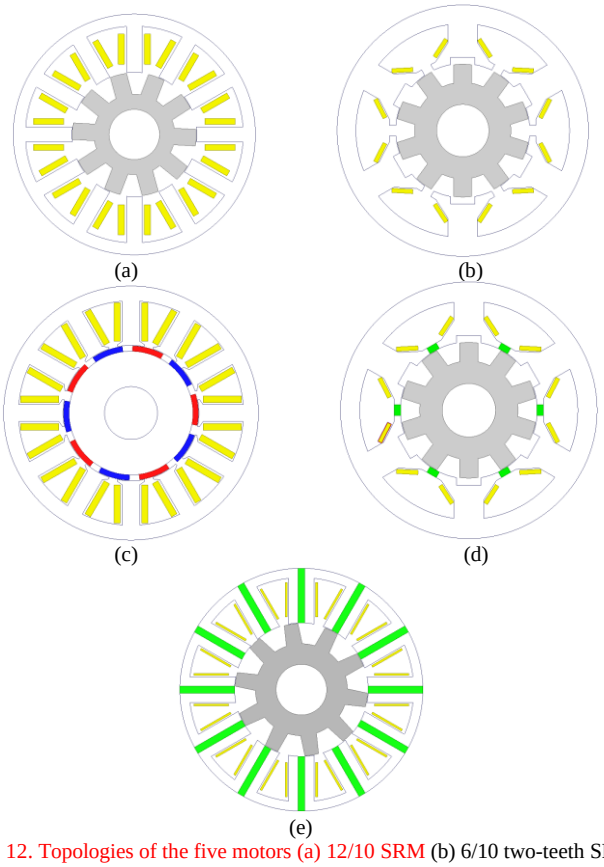

Fig. 12. Topologies of the five motors (a) 12/10 SRM (b) 6/10 two-teeth SRM (c) 12/10 BLDCM (d) 6/10 HSRM (e) 12/10 FSPM

The flux linkage curves for the three motors at the unaligned and aligned positions can be obtained from Fig. 14. It can be seen that the difference between the flux linkage values at aligned and unaligned positions for the HSRM is greater than the topology without PMs. Besides, although the difference value of the proposed motor is lower than that of 12/10 SRM, the divided teeth per stator pole can distribute the flux and produce higher reluctance torque per electrical period; as a result, the torque performance of the HSRM is not undermined. The static torque comparisons of the three topologies with the excitation current value of 5 A, 10 A and 20 A are shown in Fig. 15. (a), (b) and (c), respectively. And the total torque curves of the three motors with the rated current are displayed in Fig. 15. (d), at the speed of 1000 rpm. The square current waveform is utilized with each phase conducting half an electrical period. Because of the air cooling condition for these motors, the current density is limited to 5.5 A/mm^2 and the amplitude of the rated square current wave is around 10 A, indicating the proposed machine has the best static torque performance. Moreover, the proposed topology provides a better performance at various current values and the instantaneous torque is higher than the other two counterparts. The detailed data of the motor parameters and performance can be found in Table II. It demonstrates that the proposed HSRM can provide 64.4% and 29.8% more torque output than 12/10 SRM and 6/10 two teeth SRM, respectively. Also, the torque ripple is reduced significantly compared with 6/10 two teeth topology.

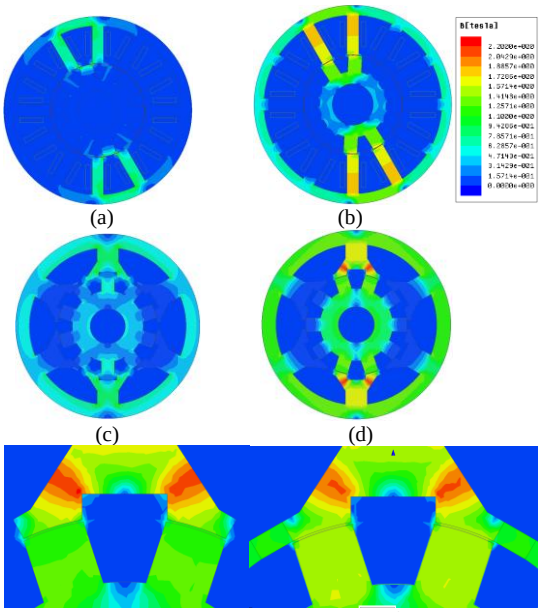

Fig. 13. Flux density of 12/10 SRM at (a) unaligned (b) aligned position
Flux density of 6/10 two-teeth SRM at (c) unaligned (d) aligned position
Airgap flux density of 6/10 two-teeth SRM at (e) unaligned (f) aligned position

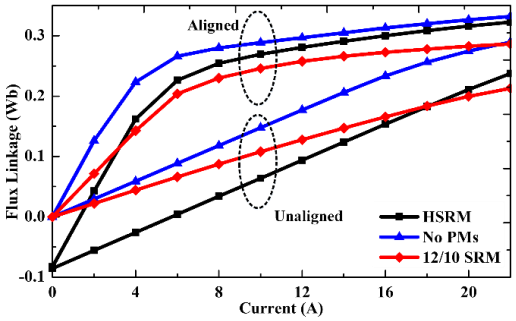

Fig. 14. Flux linkage curves of the three motors

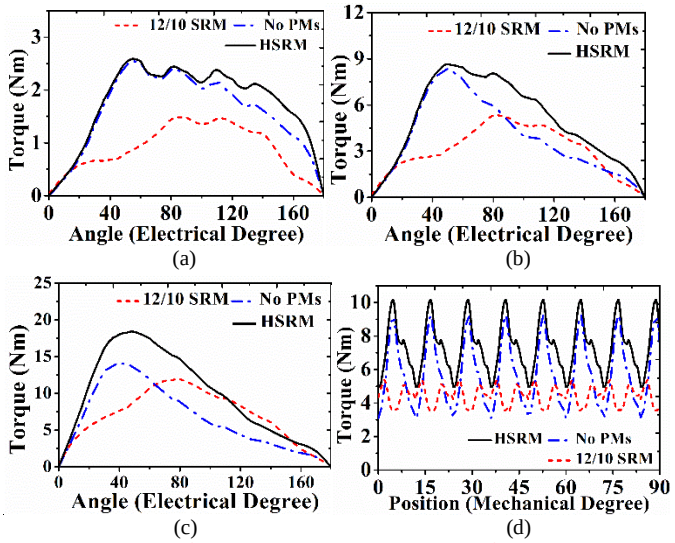

Fig. 15. Torque Performance Comparison (a) static performance at 5 A (b) static performance at 10 A (c) static performance at 20 A (d) total torque with the current density 5.5 A/mm^2

TABLE II
DIMENSION & PERFORMANCE PARAMETERS OF THE THREE MOTORS

Parameters	12/10 SRM	6/10 two-teeth SRM	6/10 HSRM
Rotor outer diameter (mm)	120	120	120
Stack length (mm)	85	85	85
Airgap length (mm)	0.3	0.3	0.3
Stator/rotor teeth arc angle (degree)	14/15	15/15.5	15/15.5
Number of turns per phase *N*	208	140	140
Slot fill factor	0.4	0.4	0.4
PM material	-	-	NdFeB35
Steel material	DW470	DW470	DW470
Rated speed (rpm)	1000	1000	1000
Current density (A/mm^2)	5.5	5.5	5.5
Rated RMS current (A)	7.1	7.1	7.1
Torque output (Nm)	4.5	5.7	7.4
Torque ripple (%)	42.4	107.3	68.5
Rated power (W)	470	590	770

The torque versus speed and power versus speed characteristics of the three motors can be obtained from Fig. 16 (a) and (b), in which, each phase is conducting during half an electric period and the dc-link voltage is fixed at 180 V. The comparison results demonstrate that the rated working point of the proposed topology is at a lower speed, and the proposed motor possesses higher torque output and stronger load capacity in the whole speed range, compared with 6/10 two teeth SRM and 12/10 SRM.

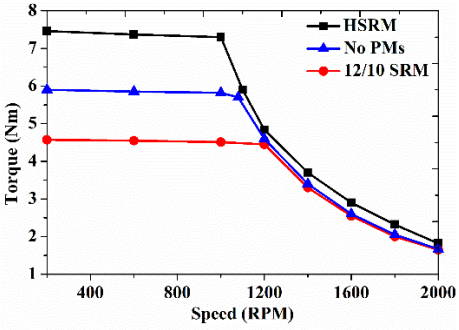

(a)

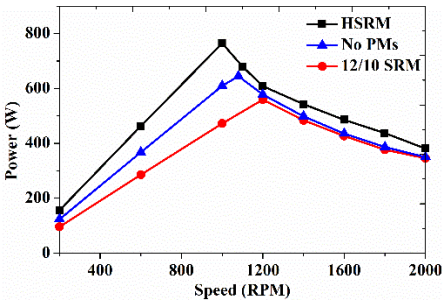

(b)

Fig. 16 (a) Torque versus speed (b) Power versus speed characteristics of the three topologies

B. Comparison with BLDCM

In order to validate the high PM utilization capability of the proposed machine, an optimized 12-slot, 10-pole three-phase six-state BLDCM is a suitable counterpart because both of them include PM material and own a similar working principle. For the BLDCM, to avoid PM demagnetization of armature reaction, it should at least satisfy $F_p>2F_i$, where F_i is MMF produced by windings around each stator pole. Therefore, the thickness of tile-shape PMs should be at least 0.9 mm. To avoid the effect of the starting current, the thickness of PMs should be double the value of its minimum. The characteristic of magnetic flux density at rated power with 1 mm thick PM is shown in Fig. 17 (a). The flux density in the stator pole is about 1.65 T. Besides, the torque and torque per PM volume versus PM thickness can be obtained from Fig. 17 (b). It indicates that when the thickness exceeds 1.8 mm, the torque value changes very little with the thickness increasing, while the torque per PM volume decreases significantly. Due to higher value of start current of the BLDCM, PMs have to be thicker to prevent demagnetization. The geometric parameters and performance data of the proposed machine and two BLDCMs with the PM thickness of 1.5 mm and 2.5 mm, can be acquired from Table III. The comparison of cogging torque can be obtained from Fig. 18 by utilizing FEA with skin depth based mesh operations.

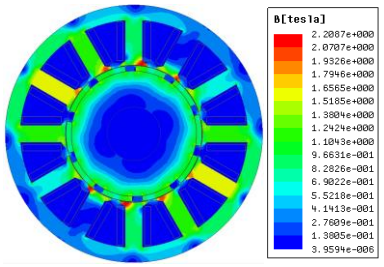

(a)

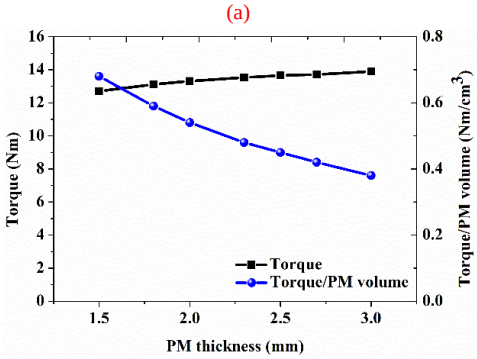

(b)

Fig. 17. (a) Flux density (b) torque characteristics curves of the BLDCM

TABLE III
PERFORMANCE DATA OF THE THREE MOTORS

Parameters & performance data	BLDCM	BLDCM	6/10 HSRM
Rotor outer diameter (mm)	120	120	120
Stack length (mm)	85	85	85
Airgap length (mm)	0.3	0.3	0.3
Number of turns per phase *N*	184	184	140
Slot fill factor	0.4	0.4	0.4
PM excitation length (mm)	1.5	2.5	5
PM arc angle (degree)	27	27	-
PM thickness (mm)	-	-	3
PM volume (cm^3)	18.60	30.49	7.65
Rated speed (rpm)	1000	1000	1000
Current density (A/mm^2)	5.5	5.5	5.5
Torque output (Nm)	12.7	13.6	7.4
Torque/PM volume (Nm/cm^3)	0.68	0.45	0.97

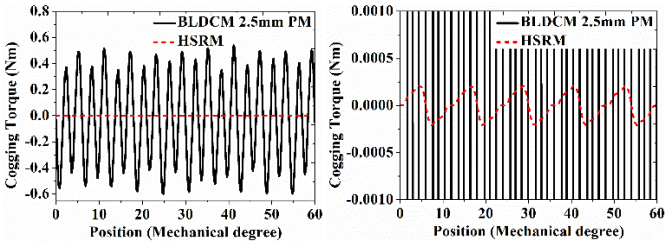

Fig. 18. (a)Overall (b) partially magnified cogging torque curves of HSRM & BLDCM

The comparison result shows that although the proposed motor is not able to output as much torque as the BLDCMs, the PM utilization factor is 43% and 116% more than the counterparts with 1.5 mm and 2.5 mm thick tile-shape PMs, respectively. Furthermore, PMs of the HSRM own a greater length in excitation direction to avoid demagnetization and the machine provides much less cogging torque.

C. Comparison with FSPM

Unlike the BLDCM with PMs on the rotor, the FSPM has a similar structure of the HSRM with PMs in the stator. Therefore, it is quite a suitable counterpart for comparison in torque performance. The design consideration of this machine is on the basis of [37] for maximum torque capability. The magnetic flux density at the rated current with the split ratio 0.55, i.e., the ratio of the inner to outer diameter of the stator, can be obtained from Fig. 19 (a). The flux density is more than 2.3 T in some parts of the stator, leading to higher magnetic reluctance and poorer utilization of PM material. The torque and torque per PM volume versus split ratio are shown in Fig. 19 (b). The FEA result indicates although the average torque for the FSPM is between 13 and 14 Nm, the torque per PM volume is only around 0.15 Nm/cm^3. The geometric parameters and performance data of the proposed machine and two FSPMs with the split ratio 0.55 and 0.60 can be acquired from Table IV. Besides, the comparison of cogging torque between the FSPM with the split ratio 0.55 and the proposed machine is shown in Fig. 20.

The result demonstrates that the proposed topology possesses a much higher PM utilization factor compared with the FSPM. Moreover, the cogging torque is reduced significantly.

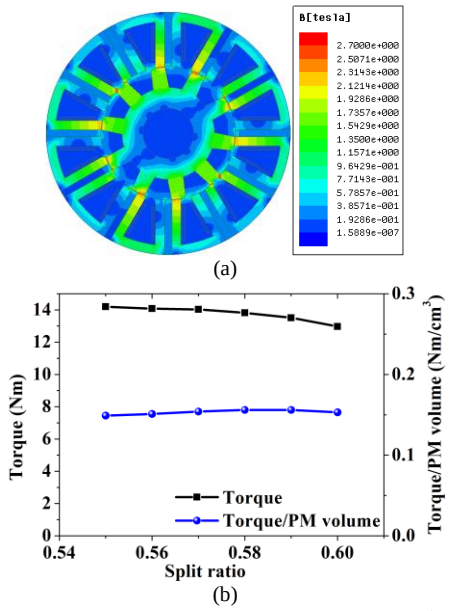

Fig. 19. (a) Flux density (b) torque characteristics curves of the FSPM

TABLE IV
PERFORMANCE COMPARISON OF THE THREE MOTORS

Parameters & performance data	FSPM	FSPM	6/10 HSRM
Rotor outer diameter (mm)	120	120	120
Stack length (mm)	85	85	85
Airgap length (mm)	0.3	0.3	0.3
Number of turns per phase *N*	144	128	140
Slot fill factor	0.4	0.4	0.4
PM excitation length (mm)	3.454	3.454	5.000
PM thickness (mm)	27.02	24.02	3
PM volume (cm^3)	95.20	84.62	7.65
Split ratio	0.55	0.60	0.53
PM arc angle (degree)	6	6	-
Stator/rotor teeth arc angle (degree)	8/12	8/12	15/15.5
Rated speed (rpm)	1000	1000	1000
Current density (A/mm^2)	5.5	5.5	5.5
Torque output (Nm)	14.2	12.9	7.4
Torque/PM volume (Nm/cm^3)	0.149	0.153	0.970

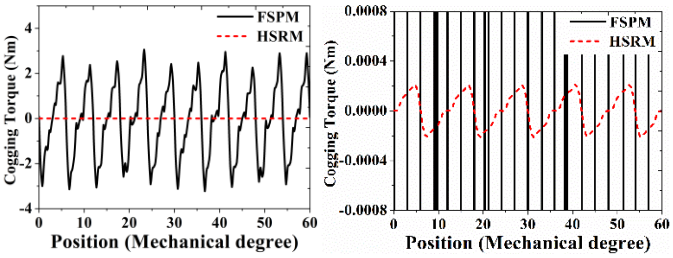

Fig. 20. (a)Overall (b) partially magnified cogging torque curves of HSRM & FSPM

VI. EXPERIMENTAL VERIFICATION

A. Static Performance Test

The static torque feature of the HSRM is measured through experiment and is compared with 2-D FEM simulation result. The field current value varies from 2 A to 10 A, along with the position covering half an electrical period from the position of non-alignment to that of alignment. The comparison result is shown in Fig. 21. It demonstrates that the experimental result corresponds well to the FEA result. The line number of the rotary encoder used for the position measurement is 2000. As

a result, the resolution can be up to 0.45 electrical degree after a four-fold increase in resolution. There is still the small error near the unaligned position due to the manufacturing error.

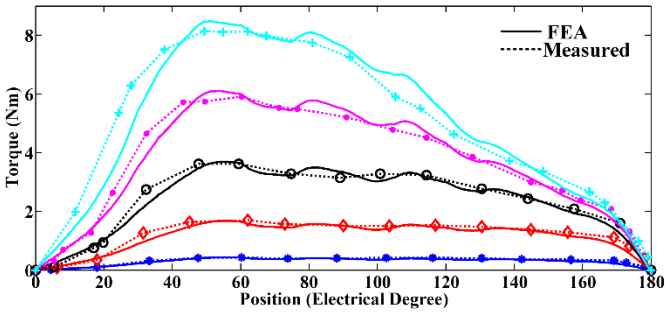

Fig. 21. Static torque performance of measurement & FEA

B. Steady Performance Test

a. Software Simulation

In order to test the steady performance of the machine, MATLAB Simulink is utilized to simulate the control system at the beginning.

The schematic of the control strategy can be obtained from Fig. 22. Dual-closed-loop control with outer speed loop and inner current loop is utilized for the control method of the proposed HSRM. PI controllers are used in both loops. The modeling process of the proposed motor is on the basis of FEM results, including the ψ-i-θ and T-i-θ curves. The waveforms of the current of phase A and torque at the speed of 220r/min and 1000r/min are shown in Fig. 23 and Fig. 24, respectively.

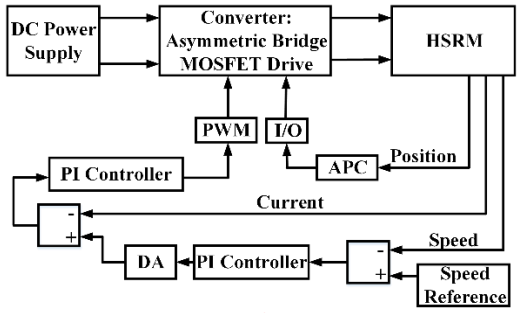

Fig. 22. Schematic of the control strategy

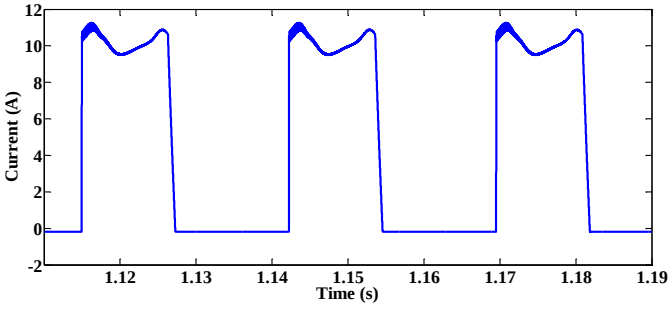

(a)

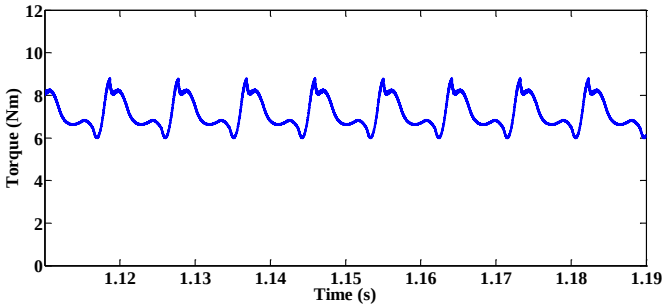

(b)

Fig. 23 (a) Current waveform of phase A (b) Total torque at the speed of 220r/min

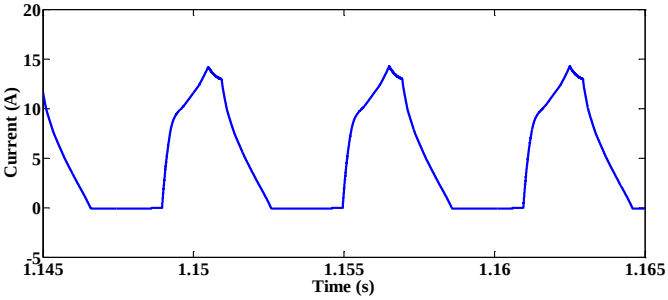

(a)

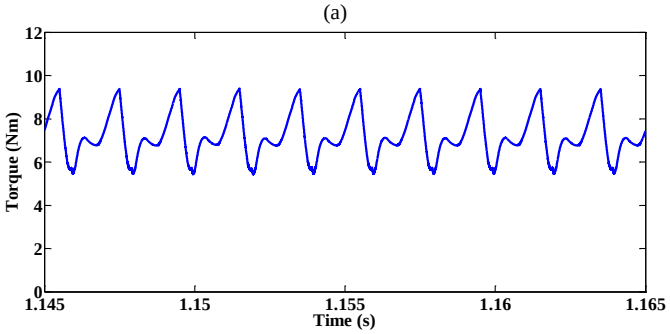

(b)

Fig. 24 Simulation waveforms (a) Current waveform of phase A (b) Total torque at the speed of 1000r/min

b. Hardware Verification

In order to confirm the theoretical analysis of the proposed topology, a prototype of a 6/10 two teeth HSRM is manufactured. The photographs of the stator, rotor and test platform are shown in Fig. 25. The type of the torque sensor is ZH07 manufactured and adjusted by Avic Power Science & Technology Engineering Co., LTD.

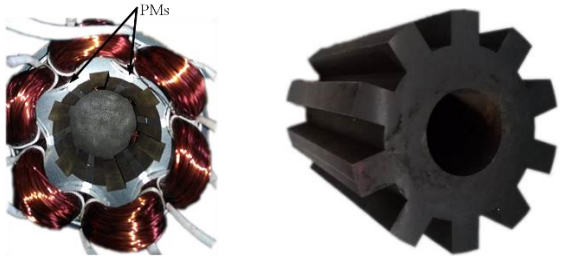

(a) (b)

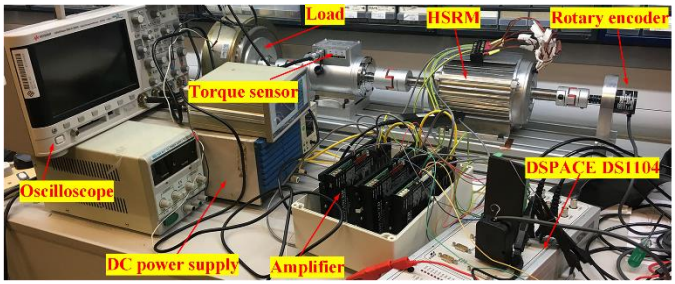

(c)

Fig. 25. Photographs of (a) stator (b) rotor (c) experimental platform setup

The HSRM is controlled by the digital controller DSPACE DS1104, via a power converter with a three-phase asymmetric half-bridge structure. For the current control, PI controller composed of the analog circuit is utilized. The transistors are selected as MOSFET to control the current value in the windings. Additionally, APC in the schematic stands for angle position control to define the turn-on and turn-off angles. The torque sensor ZH07 is utilized to measure the average torque. The DC bus voltage is set as 180 V with the turn-on angle of -0.5 degree and turn-off angle of 15 degree. Under this condition, the rated speed of the motor can reach 960 r/min. The phase waveforms at the full load current with a speed of 500 r/min are shown in Fig. 26 (a). Furthermore, when the displayer shows the average torque value of 7.3 Nm, the experimental phase current waveforms at the speed of 220 r/min and the rated speed of 960 r/min can be found in Fig. 26 (b) and (c), respectively.

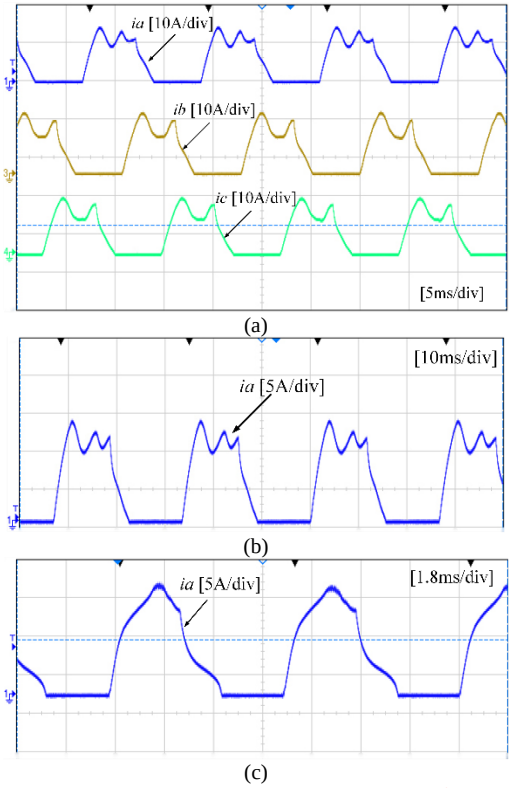

(a)

(b)

(c)

Fig. 26 Experimental results (a) Three-phase current waveform (b) Phase current & average torque waveforms of 220 r/min (c) Phase current & average torque waveforms of 960 r/min

The experimental results demonstrate that the manufactured prototype can provide the average torque output of 7.3 Nm with the current density of 5.5 A/mm^2, validating the motor design, the theoretical analysis and the FEM simulation.

C. Efficiency Test

The steady-state efficiency of the HSRM at the rated speed of 960 r/min is evaluated through experiment. The efficiency equation can be expressed as,

$$\eta = \frac{T_e \cdot \omega}{n \cdot \frac{1}{T} \sum ui \cdot \Delta t} \cdot 100\% \tag{13}$$

where n is the number of phases, u is transient voltage added to each phase, T is the total measuring time, i is the transient phase current and T_e is the average torque. The measured parameters for efficiency test can be acquired from the waveforms in Fig. 27 when the torque sensor displayer shows the average torque value of 7.3 Nm, in which Channel M is the input power of phase A.

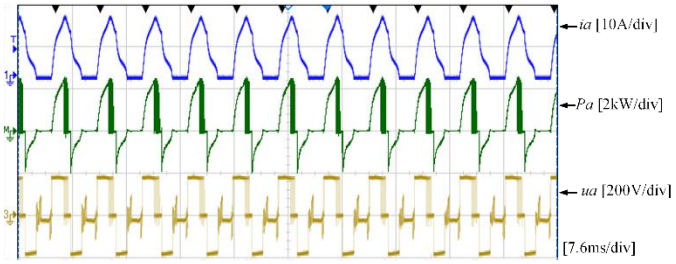

Fig. 27. Measured waveform for efficiency calculation

Therefore, the measured results illustrate that the efficiency of the proposed motor at the rated speed can reach 80.1% and output 734 W power, quite suitable for the motor of this size.

VII. Conclusion

The design considerations and performance analysis of a new 6/10 HSRM, in which PMs are inserted between adjacent stator poles of a divided teeth SRM, are presented in this paper. PMs are utilized to reduce the magnetic saturation in the stator pole and increase the flux density in the airgap.

Firstly, the working principle is analyzed theoretically. Then, the parameters of PM thickness and inner slot depth are optimized for the better torque performance and lower cost. Other motor parameters are optimized by using GA for the highest torque output and lowest torque ripple. The optimized HSRM is compared with a 12/10 SRM and a 6/10 two teeth SRM in the aspect of torque performance by using FEM simulation. The result shows the proposed machine provides much more torque than conventional 12/10 SRM and reduces torque ripple significantly compared with 6/10 two teeth SRM. Moreover, the performance comparison with a 12-slot, 10-pole three-phase six-state BLDCM and a 12/10 FSPM demonstrates that the proposed HSRM possesses a higher PM utilization factor. Finally, a prototype of the novel machine validates the motor design, the theoretical analysis and the simulation results. This study indicates the proposed HSRM has a potential for high-torque-density industrial applications.

REFERENCES

[1] K. Kiyota, and A. Chiba, "Design of Switched Reluctance Motor Competitive to 60-kW IPMSM in Third-Generation Hybrid Electric Vehicle", *IEEE Trans. Ind. Appl.*, vol. 48, no. 6, pp. 2303–2309, Nov./Dec. 2012.

[2] J. B. Bartolo, M. Degano, J. Espina, and C. Gerada, "Design and Initial Testing of a High-Speed 45-kW Switched Reluctance Drive for Aerospace Application", *IEEE Trans. Ind. Electron.*, vol. 64, no. 2, pp. 988–997, Feb. 2017.

[3] J. W. S. Jiang, B. Bilgin, and A. Emadi, "Three-Phase 24/16 Switched Reluctance Machine for a Hybrid Electric Powertrain", *IEEE Trans. Transport. Electrific.*, vol. 3, no. 1, pp. 76–85, Mar. 2017.

[4] K.Y. Lu, P. O. Rasmussen, S. J. Watkins, and Frede Blaabjerg, "A New Low-Cost Hybrid Switched Reluctance Motor for Adjustable-Speed Pump Applications", *IEEE Trans. Ind. Appl.*, vol. 47, no. 1, pp. 314–321, Jan./Feb. 2011.

[5] W. Ding, Y. F. Hu, T. Wang, and S. Yang, "Comprehensive Research of Modular E-Core Stator Hybrid-Flux Switched Reluctance Motors With Segmented and Nonsegmented Rotors", *IEEE Trans. Energy Convers.*, vol. 32, no. 1, pp. 382–393, Mar. 2017.

[6] K. Ha, C. Lee, J. Kim, R. Krishnan, and S. G. Oh, "Design and Development of Low-Cost and High-Efficiency Variable-Speed Drive System With Switched Reluctance Motor", *IEEE Trans. Ind. Appl.*, vol. 43, no. 3, pp. 703–713, May./June. 2007.

[7] S. J. Song, Z. K. Xia, Z. H. Zhang, and W. G. Liu, "Control Performance Analysis and Improvement of a Modular Power Converter for Three-Phase SRM With Y-Connected Windings and Neutral Line", *IEEE Trans. Ind. Electron.*, vol. 63, no. 10, pp. 6020–6030, Oct. 2016.

[8] F. J. P. Cebolla, A. M. Iturbe, B. Martín-del-Brío, C. Bernal, and A. B. Nuez, "Nonlinear Lumped-Circuit Model for Switched Reluctance Motors Exhibiting Core Losses", *IEEE Trans. Ind. Electron.*, vol. 63, no. 6, pp. 3433–3445, June. 2016.

[9] X. D. Xue, K. W. E. Cheng, and S. L. Ho, "A Position Stepping Method for Predicting Performances of Switched Reluctance Motor Drives", *IEEE Trans. Energy Convers.*, vol. 22, no. 4, pp. 839–847, Dec. 2007.

[10] X. D. Xue, K. W. E. Cheng, and S. L. Ho, "Online and Offline Rotary Regression Analysis of Torque Estimator for Switched Reluctance Motor Drives", *IEEE Trans. Energy Convers.*, vol. 22, no. 4, pp. 810–818, Dec. 2007.

[11] F. Peng, J. Ye, and A. Emadi, "An Asymmetric Three-Level Neutral Point Diode Clamped Converter for Switched Reluctance Motor Drives", *IEEE Trans. Power Electron.*, vol. 32, no. 11, pp. 8618–8631, Nov. 2017.

[12] W. Cai, and F. Yi, "An Integrated Multiport Power Converter With Small Capacitance Requirement for Switched Reluctance Motor Drive", *IEEE Trans. Power Electron.*, vol. 31, no. 4, pp. 3016–3026, April. 2016.

[13] K. W. Hu, J. C. Wang, T. S. Lin, and C. M. Liaw, "A Switched-Reluctance Generator With Interleaved Interface DC–DC Converter", *IEEE Trans. Energy Convers.*, vol. 30, no. 1, pp. 273–284, Mar. 2015.

[14] S. R. M. Aghdam, M. R. Feyzi, N. Bianchi, M. Morandin, "Design and Analysis of a Novel High-Torque Stator-Segmented SRM," *IEEE Trans. Ind. Electron.* , vol. 63, no. 3, pp. 1458-1466, Mar. 2016.

[15] H. Eskandari and M. Mirsalim, "An improved 9/12 two phase E-core switched reluctance machine," *IEEE Trans. Energy Convers.*, vol. 28, no. 4, pp. 951–958, Dec. 2013.

[16] B. Mecrow, E. El-Kharashi, J. Finch, and A. Jack, "Preliminary performance evaluation of switched reluctance motors with segmental rotors," *IEEE Trans. Energy Convers.*, vol. 19, no. 4, pp. 679–686, Dec. 2004.

[17] R. Vandana, S. Nikam and B. G. Fernandes, "High torque polyphase segmented switched reluctance motor with novel excitation strategy," *IET Elect. Power Appl*. vol. 6, no. 7, pp. 375-384, 2012.

[18] H. Torkaman, E. Afjei, and M. S. Toulabi, "New double-layer-per-phase isolated switched reluctance motor: Concept, numerical analysis, and experimental confirmation," *IEEE Trans. Ind. Electron.*, vol. 59, no. 2, pp. 830–838, Feb. 2012.

[19] M. Abbasian, M. Moallem, and B. Fahimi, "Double stator switched reluctance motors: Fundamentals and magnetic force analysis," *IEEE Trans. Energy Convers.*, vol. 25, no. 3, pp. 589–597, Sep. 2010.

[20] H. Arihara and K. Ataksu, "Basic properties of an axial-type switched reluctance motor," *IEEE Trans. Ind. Appl.*, vol. 49, no. 1, pp. 59–65, Jan./Feb. 2013.

[21] Y. Ebrahimi, M. R. Feyzi, "Introductory assessment of a novel high-torque density axial flux switched reluctance machine", *IET Electr. Power Appl.*, vol. 11, no. 7, pp. 1315-1323, 2017.

[22] J. Faiz, M. B. B. Sharifian, "Core Losses Estimation in a Multiple Teeth per Stator Pole Switched Reluctance Motor," *IEEE Trans. Magn.*, Vol. 30, No. 2, pp. 189-195, Mar. 1994.

[23] J. W. Zhu, K. W. E. Cheng, X. D. Xue, Y. Zou, "Design of a New Enhanced Torque In-Wheel Switched Reluctance Motor with Divided Teeth for Electric Vehicles", *IEEE Trans. Magn.*, vol. 53, no. 11, Nov. 2017.

[24] Z. X. Xiang, L. Quan, and X. Y. Zhu, "A New Partitioned-Rotor Flux-Switching Permanent Magnet Motor With High Torque Density and Improved Magnet Utilization", *IEEE Trans. Appl. Supercond.*, vol. 26, no. 4, Jun. 2016.

[25] T. J. Zou, D. W. Li, R. H. Qu, D. Jiang, and J. Li, "Advanced High Torque Density PM Vernier Machine with Multi Working Harmonics", *IEEE Trans. Ind. Appl.*, vol 53, no. 6, pp. 5295-5304, Nov./Dec. 2017.

[26] E. Hoang, A. H. B. Ahmed, J. Lucidarme, "Switching Flux Permanent Magnet Polyphased Synchronous Machines", 7th European Conference on Power Electronics and Applications, Trondheim, Norway, 1997.

[27] W. Hua, G. Zhang, and M. Cheng, "Investigation and Design of a High-Power Flux-Switching Permanent Magnet Machine for Hybrid Electric Vehicles", *IEEE Trans. Magn.*, vol. 51, no. 3, Mar. 2015.

[28] Z. Q. Zhu and J. T. Chen, "Advanced Flux-Switching Permanent Magnet Brushless Machines", *IEEE Trans. Magn.*, vol. 46, no. 6, pp. 1447-1453, Jun. 2010.

[29] P. Andrada, B. Blanqué, E. Martínez, and M. Torrent, "A Novel Type of Hybrid Reluctance Motor Drive", *IEEE Trans. on Ind. Electron.*, vol. 61, no. 8, pp. 4337 - 4345, Aug. 2014.

[30] Y. Hasegawa, K. Nakamura, and O. Ichinokura, "A Novel Switched Reluctance Motor with the Auxiliary Windings and Permanent Magnets", *IEEE Trans. Magn.*, vol. 48, no. 11, pp. 3855 – 3858, Nov. 2012.

[31] W. Ding , S. Yang, Y. F. Hu , S. Li, T. Wang, and Z. G. Yin, "Design Consideration and Evaluation of a 12/8 High-Torque Modular-Stator Hybrid Excitation Switched Reluctance Machine for EV Applications", *IEEE Trans. Ind. Electron.*, vol. 64, no. 12, pp. 9221–9232, Dec. 2017.

[32] J. F. Lindsay, R. Arumugam, R. Krishnan, "Finite-element analysis characterization of a switched reluctance motor with multitooth per stator pole," *IEE Proceedings B, Elect. Power. Appl.* vol. 133, no. 6, pp. 347-353, Nov. 1986.

[33] E. Severson, R. Nilssen, T. Undeland, and N. Mohan, "Magnetic Equivalent Circuit Modeling of the AC Homopolar Machine for Flywheel Energy Storage", *IEEE Trans. Energy Convers.*, vol. 30, no. 4, pp. 1670–1678, Dec. 2015.

[34] W. Peng and J. Gyselinck, "Magnetic-equivalent-circuit modelling of switched reluctance machines with mutual coupling effects," in *Proc. Int. Conf. Elect. Mach.*, Sep. 2016, pp. 426–432.

[35] X. D. Xue, K.W.E. Cheng, T. W. Ng, and N. C. Cheung, "Multi-Objective Optimization Design of In-Wheel Switched Reluctance Motors in Electric Vehicles", *IEEE Trans. Ind. Electron.*, vol. 57, no. 9, pp. 2980 – 2987, Sep. 2010.

[36] R. Krishnan, "Steady-State Performance and Analytic Derivation of SRM Characteristics" in Switched Reluctance Motor Drives—Modeling, Simulation, Analysis, Design, and Applications. Boca Raton, FL: CRC Press, 2001, ch. 2.

[37] Z. Q. Zhu, Y. Pang, D. Howe, S. Iwasaki, R. Deodhar, and A. Pride, "Analysis of Electromagnetic Performance of Flux-Switching Permanent-Magnet Machines by Nonlinear Adaptive Lumped Parameter Magnetic Circuit Model", *IEEE Trans. Magn.*, vol. 41, no. 11, pp. 4277-4287, Nov. 2005.

Jingwei Zhu was born in Liaoning, China. He received the B.E. degree in Electrical Engineering & Automation, Zhejiang University, Hangzhou, China, in 2015 and the M.Phil. degree in Electrical Engineering, The Hong Kong Polytechnic University, Hong Kong, in 2018. He is awarded an ECE 2018 Chancellors Opportunity Fellowship (COF) to support his Ph.D. study in Wisconsin Electric Machines and Power Electronics Consortium (WEMPEC), University of Wisconsin-Madison. His research interests including design of novel electric machines, motor drives and power electronics.

Ka Wai Eric Cheng (M'90-SM'06) received the B.Sc. and Ph.D. degrees from the University of Bath, Bath, U.K., in 1987 and 1990, respectively.

Before joining the Hong Kong Polytechnic University, Kowloon, Hong Kong, in 1997, he was with Lucas Aerospace, U.K., as a Principal Engineer, where he led a number of power electronics projects. He has written more than 250

papers and 7 books. He is currently the Professor and Director of Power Electronics Research Centre, Hong Kong Polytechnic University.

Dr. Cheng research interests include all aspects of power electronics, motor drives, electromagnetic interference, electric vehicle, battery management, and energy saving. Dr. Cheng received the IEE Sebastian Z De Ferranti Premium Award in 1995, the Outstanding Consultancy Award in 2000, the Faculty Merit Award for best teaching in 2003 from the Hong Kong Polytechnic University, the Faculty Engineering Industrial and Engineering Services Grant Achievement Award in 2006, the Brussels Innova Energy Gold Medal with Mention in 2007, the Consumer Product Design Award in 2008, the Electric Vehicle Team Merit Award of the Faculty in 2009, Geneva Invention Expo Silver Medal in 2011 and Eco Star Award in 2012, Gold Prize in super-capacitor, at Seoul International Invention (2015) and iCAN 2016 for contribution in active suspension.

Xiangdang Xue (M'10–SM'12) obtained his B.Eng. degree from Hefei University of Technology, Hefei, Anhui, China, in 1984, his M.Eng. degree from Tianjin University, Tianjin, China, in 1987, and his Ph.D. degree from the Hong Kong Polytechnic University, Hong Kong, China, in 2004, all in electrical engineering.

Dr. Xue engaged in teaching and research in Department of Electrical Engineering, Tianjin University, China, from 1987 to 2001, as a lecturer and an associate professor. He is currently with Department of Electrical Engineering, the Hong Kong Polytechnic University, as a research fellow.

Dr. Xue's research interests are in the areas of electrical machines, electrical drives, power electronics, and energy storage systems. He has published over 100 papers. His current research is focused on energy storage components, battery management systems, electric vehicles, switched reluctance motor drives, and high frequency AC. Dr. Xue received the Electric Vehicle Team Merit Award of the Faculty in 2009, the Gold Prize in super-capacitor at Seoul International Invention Fair (2015), and the Gold Medal for contribution in active suspension at iCAN 2016.